DC to High-Frequency HBT-Model Parameter Evaluation Using Impedance Block Conditioned Optimization

Apostolos Samelis and Dimitris Pavlidis, *Fellow, IEEE*

***Abstract*— A new heterojunction bipolar transistor (HBT) small-signal equivalent-circuit parameter-extraction procedure employing multibias S-parameter data is presented. The algorithm combines analytical and empirical parameter evaluation techniques and results in a bias-dependent HBT model. To minimize the risk of nonphysical parameter estimation, elements such as the dc transport factor, α_o, and the emitter–base conductance are evaluated from the device dc characteristics, and the frequency dispersion of α is related to the RC time-constant of the emitter–base junction. Moreover, initial values for the extrinsic device parasitics are obtained from "hot" as well as "cold" S-parameter data. The method results in excellent fit between measured and modeled S-parameter data in the frequency range dc-40 GHz and for a wide range of bias operating points.**

***Index Terms*— Analytical techniques, heterojunction bipolar transistors, small-signal analysis.**

I. Introduction

HETEROJUNCTION bipolar transistors (HBT's) have demonstrated their suitability for a multitude of electronic applications. As the range of applications constantly widens, ranging from analog power to digital circuits [1], [2], the need for accurate HBT models is a key factor for their successful employment in systems.

Physically significant HBT models offer one the ability not only to predict and to design a practical circuit with great accuracy, but also to estimate the device parameters affecting high-frequency (HF) performance. This could allow the evaluation of the manufacturing process and address the optimization of device design with respect to a particular application.

HBT equivalent-circuit parameter-extraction methods have been developed by many researchers in the past. A systematic procedure was presented in [3], where all HBT parameters were extracted using test structures for the estimation of the device parasitics. Low- and HF network parameters were used for the extraction of the intrinsic and parasitic HBT-model components, respectively, in [4], employing both analytic and empirical fitting procedures. The technique presented in [5] employed the total emitter–to–collector delay time obtained from the cutoff frequency, to constrain the model elements. Using "open" and "shorted" test structures, initial estimates were obtained for the HBT parasitics in [6], which were used in the optimization of HBT models. The latter approach was further supported through the utilization of cutoff mode S-parameter data in [7] as well as HBT dc parameters obtained from device Gummel-plots [8]. An all-analytic approach was developed for the first time in [9], in which the frequency dependence of equivalent circuit-impedance blocks derived from device S-parameter data was utilized allowing direct evaluation of all HBT parameters. This method was slightly modified in [10] to include the effect of external parasitic capacitances obtained from "cold" S-parameter data. More recently, a different approach was established in [11] where all elements were obtained by analytic expressions derived under certain assumptions. An analytic HBT parameter technique based on the approach developed in [9] and accounting for a distributed base-collector capacitance was presented in [12]. Finally, a direct extraction procedure of HBT elements was developed in [13] where S-parameter data measured under open-collector bias conditions were utilized to derive the extrinsic device parasitics and a distributed base resistance was accounted for.

All direct HBT parameter-extraction methods [9]–[13] predict some of the HBT parameters through assumptions based on the frequency behavior of the deembeded equivalent circuit-impedance blocks. Their great advantage is their speed as well as the physical importance of the obtained parameters. Their disadvantage is, however, the fact that their formalism is developed with respect to a particular model topology. Consequently, their applicability for a variety of devices with different designs may be compromised in a case where the model topologies associated with these approaches are insufficient to describe device behavior. In such a case, additional elements need to be incorporated into the HBT model in order to facilitate device modeling at high frequencies. Consequently, new extraction methodologies associated with the new model are required, which, depending on the circuit complexity, may result in complicated formulations. A cumbersome effort would then be required to elaborate on appropriate assumptions and derive expressions that allow the direct evaluation of the equivalent circuit elements.

Manuscript received January 26, 1996; revised February 28, 1997. This work was supported by ARO under Contract DAAL 03-92-G-0109 and MAFET/Westinghouse under Contract N00014-95-C-6026.

A. Samelis was with the Solid State Electronics Laboratory, Department of Electrical Engineering and Computer Science, University of Michigan, Ann Arbor, MI 48109-2122 USA.. He is now with Rockwell Semiconductor Systems, Newbury Park, CA 91320 USA.

D. Pavlidis is with the Solid State Electronics Laboratory, Department of Electrical Engineering and Computer Science, University of Michigan, Ann Arbor, MI 48109-2122 USA.

Publisher Item Identifier S 0018-9480(97)03910-0.

In this paper, the difficulties mentioned above were avoided by developing a new procedure for the extraction of the HBT parameters based on both empirical and analytical evaluations. The HBT equivalent circuit employed here includes parasitic extrinsic capacitances and inductors. Due to the complexity of this circuit, the parameter evaluation procedure is semi-analytic, i.e., it self-consistently couples analytical derivations (for the internal HBT model) and empirical fittings (for the external HBT parasitics). To enhance the physical importance of the obtained parameters, the optimization of multibias S-parameter data is carried out simultaneously, some of the HBT elements are constrained ($g_{\rm BE}$, α_0) or initialized (R_E, R_C, R_B) according to the device dc behavior and initial values for the extrinsic parasitics are estimated from "hot" and "cold" data. Section II presents the dc-parameter extraction procedure. The HBT small-signal equivalent circuit is presented in Section III. Section IV deals with the determination of the initial values of the extrinsic parasitics. In Section V, the new HBT small-signal parameter-extraction method is presented and results are discussed in Section VI.

II. HBT DC Model Parameter Extraction

In this paper, a procedure for the extraction of the Ebers–Moll dc parameters was developed. The procedure employs Newton–Raphson iterations and avoids using matrix manipulations based on singular value decomposition employed in [14]. The dc parameters will be used later on for the evaluation of bias-dependent small-signal HBT-model parameters such as $g_{\rm BE}$ and α_0 and the initialization of the device series resistances R_E, R_B, and R_C. Such parameters can be used in HBT large-signal modeling continuously from dc to microwave frequencies provided that no dispersion effects take place in the MHz frequency regime due to thermal time constants.

The parameters required by this model are:

- forward saturation current (I_S), forward ideality factor (η_f), emitter series resistance (R_E);
- reverse saturation current $(I_{\rm SR})$, reverse ideality factor (η_r), base and collector series resistances (R_C, and R_B, respectively);
- forward current gain (β_f), emitter space–charge region recombination saturation current $(I_{\rm SE})$, and its ideality factor (η_e);
- reverse current gain (β_r), collector space–charge region recombination saturation current $(I_{\rm SC})$, and its ideality factor (η_c).

Each set of parameters is determined separately and their derivation will now be described.

The device under study was an AlGaAs/GaAs HBT consisting of nine cells, each having two emitter fingers of 2×20 μm^2 area. The forward collector current was utilized for the extraction of I_S, η_f, and R_E. The approach is based on the assumption that the bias dependence of this current is given by the following equation:

$$I_C = I_S \exp\left[\frac{V_{\rm BE} - I_B R_B - (I_C + I_B)R_E}{\eta_f V_T}\right]. \quad (1)$$

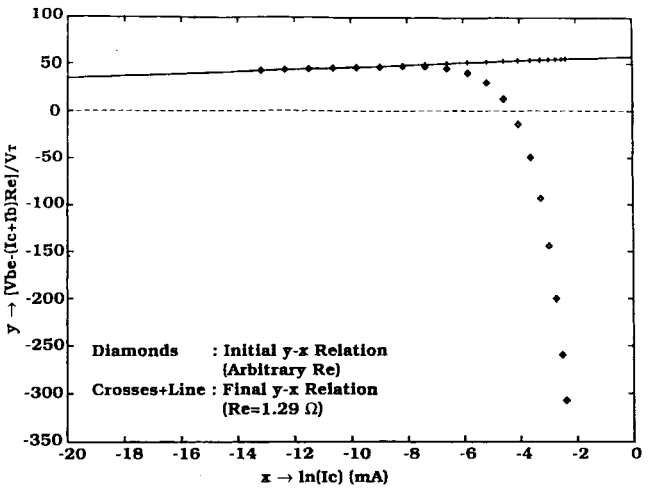

Fig. 1. Initial and final y–x relation. Slope and y-axis ($x = 0$) intercept of final linearized relation are equal to η_f and $-\eta_f \ln(I_S)$, respectively.

One could easily account for thermal effects by adding $V_{\rm th} = \delta R_{\rm th}(I_C V_{\rm CE} + I_B V_{\rm BE})$ to $V_{\rm BE}$ in the above equation, where $R_{\rm th}$ is the thermal resistance of the device and δ is the temperature coefficient of $V_{\rm BE}$. This would lead to a larger value for R_E compared to the case where no thermal effects are accounted for. Effects of this type were not considered in the analysis of the device described in this paper.

Since the forward I_C is usually much larger than I_B, an assumption that the voltage drop across R_B is much less than the voltage drop across R_E can be made, and (1) can be simplified to

$$I_C = I_S \exp\left[\frac{V_{\rm BE} - (I_C + I_B)R_E}{\eta_f V_T}\right]. \quad (2)$$

Consequently, (2) can be rewritten in the form

$$y = -\eta_f \ln(I_S) + \eta_f x \quad (3)$$

where

$$x = \ln(I_C) \quad (4)$$

$$y = \frac{V_{\rm BE} - (I_C + I_B)R_E}{V_T} \quad (5)$$

and $V_T = k_B T/q = 0.0259$ V. Obviously, the above assumption is valid only for devices with sufficiently high dc-current gain. To evaluate I_S, η_f, and R_E based on (3)–(5), one first obtains the sets of x and y quantities based on the device forward Gummel-plot. The relation between x and y is linear only if the correct value of R_E is used. One possible approach, therefore, for determining R_E is to linearize the y versus x relationship using an appropriate value for R_E. This can be done numerically without any complications by fitting y and x to a second-order polynomial using least-square fitting techniques and solve the equation $c_2(R_E) = 0$, where $c_2(R_E)$ is the second-order expansion coefficient of the y versus x relationship. The Newton–Raphson-based scheme employed here converges within a few iterations and yields a unique

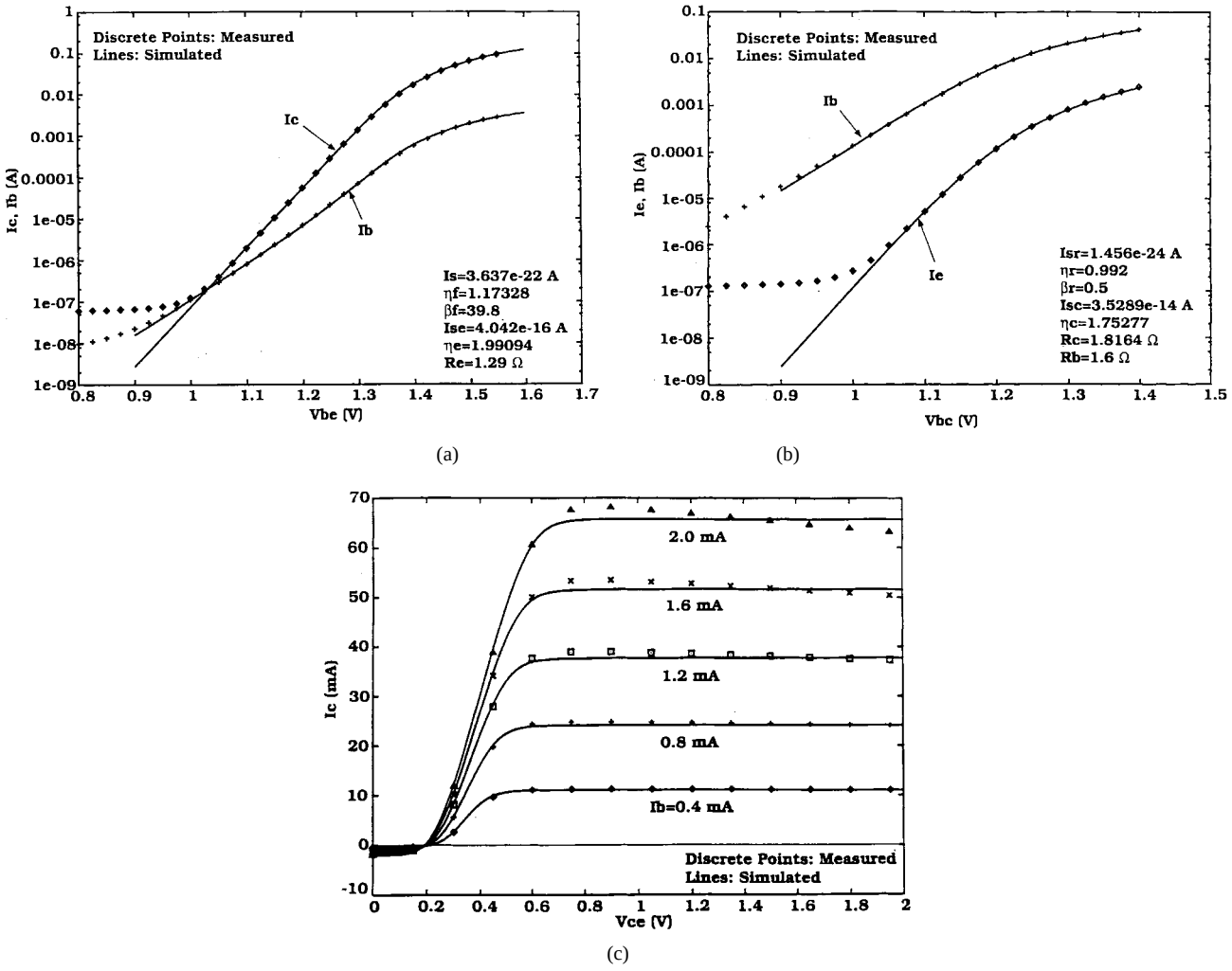

Fig. 2. (a) Measured and modeled forward Gummel-plots of 360 μm^2 AlGaAs/GaAs HBT. (b) Measured and modeled reverse Gummel-plots of 360 μm^2 AlGaAs/GaAs HBT. (c) Measured and modeled $I_C - V_{CE}$ characteristics of 360 μm^2 AlGaAs/GaAs HBT.

solution for R_E. Based on (3), one also sees that η_f and I_S can then be found easily from the slope and y-axis intercept of the final y–x relation. Fig. 1 shows the initial and final y–x relation after the linearization of y–x by R_E is accomplished.

The reverse Gummel-plot related parameters, I_{SR}, η_r, and $R_B + R_C$ can also be found following a similar procedure. It must be noticed that here, one calculates the sum of R_B and R_C, which is true if I_B is much larger than I_E under reverse HBT operation.

In the extended Ebers–Moll model, the base current consists of two components, one accounting for bulk recombination in the quasi-neutral base (I_S/β_f) and the other accounting for space–charge recombination (I_{SE}) or, in general, any leakage mechanism. The parameters to be determined for the base current are β_f, I_{SE}, and η_e (forward mode) and β_r, I_{SC}, and η_c (reverse mode).

An optimization routine similar to the one presented above was also developed for the calculation of base–current parameters for each mode of operation. For the forward base current one writes

$$I_B = \frac{I_C}{\beta_f} + I_{SE}\left\{\exp\left[\frac{V_{BE} - (I_C + I_B)R_E}{\eta_e V_T}\right] - 1\right\}. \quad (6)$$

This can be casted in the following convenient form:

$$y = -\eta_e \ln(I_{SE}) + \eta_e x \quad (7)$$

where

$$x = \ln\left(I_B - \frac{I_C}{\beta_f}\right) \quad (8)$$

and

$$y = \frac{V_{BE} - (I_C + I_B)R_E}{V_T}. \quad (9)$$

β_f can, therefore, be found by modifying it until the y–x relationship has been linearized. The other two unknown parameters, I_{SE} and η_e, are obtained by evaluating the slope and y-axis intercept of the linearized y–x relation.

A similar procedure can also be established for the reverse operating conditions, yielding in this case the I_{SC}, η_c, and β_r values.

The individual R_C and R_B values can finally be estimated by adjusting R_C, while keeping $R_C + R_B$ constant, until a good fit of the device $I_C - V_{CE}$ characteristic in the saturation region is obtained.

The device forward and reverse Gummel-plots are shown in Fig. 2(a) and (b), respectively. Excellent agreement is

TABLE I
EBERS–MOLL DC MODEL PARAMETERS

Parameter	Value	Parameter	Value
I_S	$3.637 \cdot 10^{-22}$ A	η_f	1.17328
I_{SR}	$1.456 \cdot 10^{-24}$ A	η_r	0.992
β_f	39.8	β_r	0.5
I_{SE}	$4.042 \cdot 10^{-16}$ A	η_e	1.99094
I_{SC}	$3.5289 \cdot 10^{-14}$ A	η_c	1.75277
R_C	1.8164 Ω	R_E	1.29 Ω
R_B	1.6 Ω		

observed between measured and modeled dc characteristics. The experimentally measured and theoretically estimated $I_C - V_{\rm CE}$ characteristics of the device are shown in Fig. 2(c) and also show excellent agreement. It should be mentioned that thermal effects causing discrepancies at high bias conditions were not incorporated in the dc model. Table I shows all dc model parameters obtained from this procedure. The above procedure was successfully used for a variety of devices employing different emitter geometries and material systems.

III. HBT SMALL-SIGNAL EQUIVALENT CIRCUIT

The HBT small-signal equivalent circuit employed in this paper has the T-model configuration and is shown in Fig. 3(a). It is divided into three sub-shells, each of which is treated in a different fashion. The *analytic* HBT shell is evaluated analytically, i.e., its impedance blocks are derived directly from the deembeded S-parameters provided that the elements surrounding it can be evaluated by other techniques i.e., "cold" tests, etc. The Z'-shell surrounds the *analytic* shell through the external parasitic capacitances C_{p1}, C_{p2}, and C_{px}. Finally, the entire device is defined through the external series parasitic impedances $Z_{bx} = R_{bx} + j\omega L_{bx}$, $Z_{ex} = R_{ex} + j\omega L_{ex}$, and $Z_{cx} = R_{cx} + j\omega L_{cx}$ surrounding the Z'-shell.

The circuit schematic for the *intrinsic* HBT is shown in Fig. 3(b). The transport factors α and α' are given by

$$\alpha = \frac{a_0}{1 + j\omega \frac{C_{\rm BE}}{g_{\rm BE}}} \exp(-j\omega\tau_d) \tag{10}$$

and

$$\alpha' = \frac{a_0}{1 + j\omega \frac{C_{\rm BE}+C_{\rm JE}}{g_{\rm BE}}} \exp(-j\omega\tau_d). \tag{11}$$

α_0 is the dc transport factor, $C_{\rm BE}$ and $C_{\rm JE}$ are the emitter–base diffusion and transition capacitances, respectively, $R_{\rm be}\,(g_{\rm BE})$ is the emitter–base resistance (conductance), $C_{\rm bc}$ is the base-collector capacitance, $R_{\rm bc}$ is the base-collector resistance, and τ_d is a phase delay associated with carrier transit through both the base and the collector. It must be noted here that the above form for α is not the same as in [9]. The pole of α employed in [9] was $\omega_0 = \frac{\pi^2}{8\tau_B} \approx \frac{1.233}{\tau_B}$. τ_B is the base transit time and is related to $C_{\rm BE}$ and $g_{\rm BE}$ by $\tau_B \equiv C_{\rm BE}/g_{\rm BE}$ under quasi-static approximation and $\tau_B \equiv \frac{3}{2}C_{\rm BE}/g_{\rm BE}$ under nonquasi-static approximation [15]. In this paper, the form $\omega_0 = g_{\rm BE}/C_{\rm BE}$ was adopted. This form was chosen instead of that in [9] to ensure consistency of the small-signal model with the Gummel–Poon large-signal model defined in commercial circuit simulators. Small-signal circuits corresponding to such large-signal models, when transformed into the T-model configuration result in transport factors like the one given by (10) and (11). Furthermore, adopting such forms for α and α' subjects this procedure into its first constraint—namely, that the pole f_a of α' can be related to the emitter–base elements through $f_a = \frac{1}{2\pi R_{\rm bc}(C_{\rm BE}+C_{\rm JE})}$.

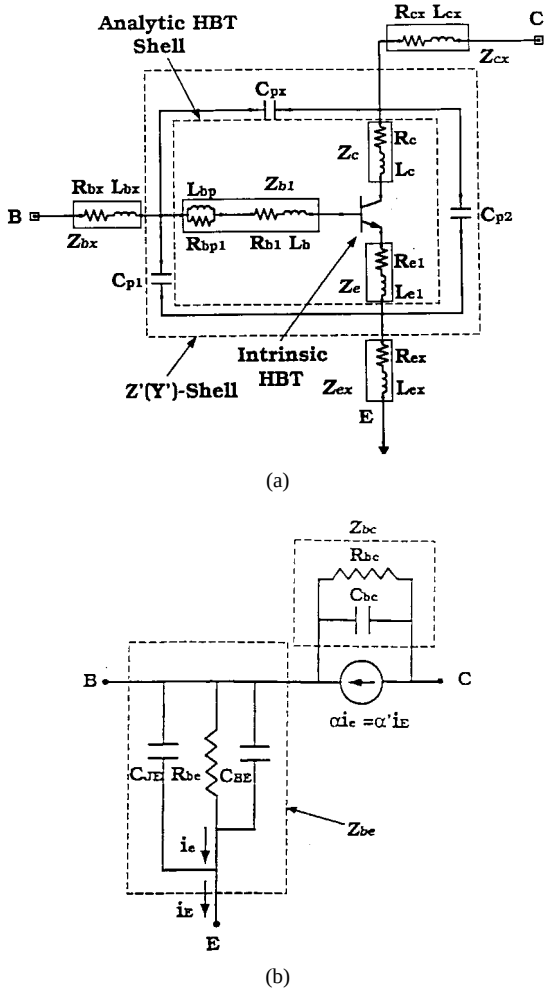

Fig. 3. (a) HBT small-signal equivalent circuit. (b) *Intrinsic* HBT schematic.

IV. INITIALIZATION OF EXTERNAL PARASITICS

The external parasitics of the HBT model of Fig. 3(a) are the parasitic interconnect pad capacitances C_{p1}, C_{p2}, and C_{px} and the impedances $Z_{bx} = R_{bx} + j\omega L_{bx}$, $Z_{ex} = R_{ex} + j\omega L_{ex}$, and $Z_{cx} = R_{cx} + j\omega L_{cx}$. Since the parameter evaluation procedure developed in this paper employs empirical optimization techniques, it is desired that the above elements be properly initialized. The extraction procedures described below served in obtaining initial values of device parasitics. The exact values of such parasitics were obtained after the optimization procedure was completed. It should be mentioned here that open/short interconnect structures [6] as well as single-cell HBT's could assist the estimation of the pad parasitics. Such structures are, however, not always available as was the case for the HBT's studied in this paper. The parasitics were, therefore, estimated using the device structure itself as explained below.

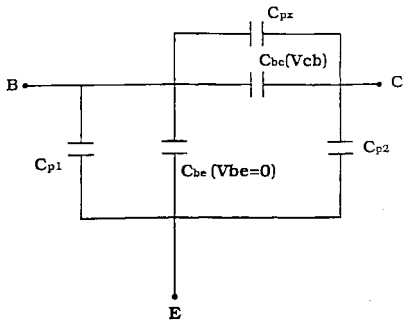

Fig. 4. HBT equivalent circuit under cutoff operation (zero $V_{\rm BE}$, zero I_C, variable $V_{\rm CB}$), and for low frequencies.

C_{p1}, C_{p2}, and C_{px} can be evaluated from HBT behavior at low frequencies (0–10 GHz) and cutoff operating conditions (zero $V_{\rm BE}$, zero I_C, variable $V_{\rm CB}$). Under such conditions, the HBT equivalent circuit of Fig. 3(a) and (b) exhibits full capacitive behavior and is simplified as shown in Fig. 4.

In such a case, the device capacitances can be calculated directly by

$$C_{p1}+C_{be,V_{\rm bc}=0}=\frac{{\rm Im}[Y_{11}]+{\rm Im}[Y_{12}]}{\omega} \tag{12}$$

$$C_{p2}=\frac{{\rm Im}[Y_{22}]+{\rm Im}[Y_{12}]}{\omega} \tag{13}$$

and

$$C_{{\rm bc}x}=-\frac{{\rm Im}[Y_{12}]}{\omega}\equiv C_{px}+C_{\rm bc}. \tag{14}$$

The first two quantities obtained from the "cold" S-parameter data were found independent on $V_{\rm CB}$ and had the values of $C_{p1}+C_{{\rm be},V_{\rm bc}=0}=518.22$ fF ($C_{\rm be}$ is the total base–emitter capacitance, i.e., $C_{\rm be}=C_{\rm BE}+C_{\rm JE}$) and $C_{p2}=96.54$ fF. $C_{{\rm bc}x}$ is a bias-dependent quantity, which can be modeled through a constant capacitance C_{px} and a bias dependent capacitance $C_{\rm bc}$. A suitable expression for $C_{\rm bc}$ is given by

$$C_{\rm bc}=\frac{C_{\rm bco}}{\sqrt{1+V_{\rm cb}/V_{\rm jco}}}. \tag{15}$$

The above relation is suitable for HBT's whose collector depletion region is not fully depleted and is valid for the range of applied reverse base-collector bias ($V_{\rm cb}<6$ V) employed in this study. In case of extreme bias conditions, however, one should employ more general expressions for the bias dependence of $C_{\rm bc}$ [16]. The extraction of the parameters $C_{\rm bco}$, $V_{\rm jco}$, and C_{px} is carried out adopting a procedure similar to the one used earlier for the extraction of the dc-model parameters. One reiterates in this case, the above relation as

$$y\equiv\frac{1}{(C_{{\rm bc}x}-C_{px})^2}=\frac{1}{C_{\rm bco}^2}+\frac{1}{C_{\rm bco}^2V_{\rm jco}}x \tag{16}$$

where $x\equiv V_{\rm cb}$. Thus, the above y versus x relation can be linearized by choosing a proper value for C_{px}, which for the case of the device under study was $C_{px}=172$ fF. Once the proper C_{px} is determined, the remaining two parameters can be evaluated from the slope and intercept of the final linearized y–x relation. These were determined as $C_{\rm bco}=133.63$ fF and $V_{\rm jco}=1$ V.

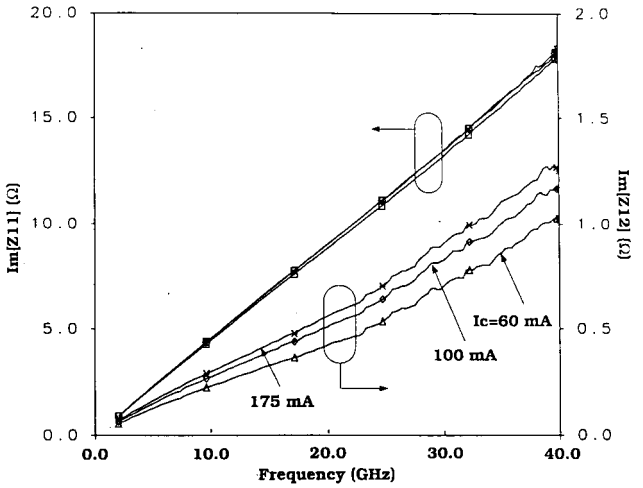

Fig. 5. Imaginary part of Z_{11} and Z_{12} under forward operating conditions.

At this point, it must be noted that all the capacitive components derived so far can be used to initialize the corresponding model elements of Fig. 3(a). However, since their derivation is based on low-frequency data, their location in the circuit model can be defined arbitrarily. For example, C_{px} appears in the circuit schematic of Fig. 3(a) to be a parasitic feedback capacitance externally defined with respect to the *analytic* HBT. However, C_{px} could equally well represent the collector–base capacitance under complete collector region depletion conditions (high reverse $V_{\rm BC}$). This would dictate the incorporation of C_{px} in parallel to the *intrinsic* HBT collector–base capacitance rather than externally as shown in Fig. 3(a). Thus, one has different options for the choice of the initial value of C_{px}, ranging from 0 to 172 fF. In this paper, the initial value for C_{px} was chosen to be zero, i.e., it was assumed that all C_{px} is absorbed by the collector–base capacitance of the *intrinsic* HBT. Such an initial value was found to improve the convergence and speed of the parameter estimation algorithm to be presented next. Similar arguments can be made about the nature of C_{p1}. The initial value of this capacitance was chosen to be equal to 518.22 fF. As will now be shown, this value appears to be high and most of C_{p1} is absorbed by the emitter–base junction capacitance of the *intrinsic* HBT. Finally, the initial value for C_{p2} was maintained at 96.54 fF as determined above, since no intrinsic device capacitance exists which is in parallel to C_{p2} and could absorb the effects of C_{p2}, as in the case of C_{p1} or C_{px}.

The initialization of the series inductors of the HBT model can also be addressed using "hot" S-parameter data (nonzero I_C, modest $V_{\rm CE}$). One can, in this case, use the device measured Z-parameters. With respect to Fig. 3(a) and assuming at a first approximation zero R_{ex}, R_{cx}, and R_{bx} due to the negligible device interconnect resistivity, one can write

$$Z_{11}=Z'_{11}+j\omega(L_{bx}+L_{ex}) \tag{17}$$

$$Z_{12}=Z'_{12}+j\omega L_{ex}. \tag{18}$$

The imaginary part of the measured Z-parameters ${\rm Im}[Z_{11}]$ and ${\rm Im}[Z_{12}]$ showed linear dependence on frequency for the

device under study as shown in Fig. 5. As can be seen, $\mathrm{Im}[Z_{11}]$ is independent on the collector current suggesting a strong contribution by the inductive components of the HBT model. In the case of $\mathrm{Im}[Z_{12}]$, a stronger bias dependence is observed. This bias dependence is attributed to the bias dependent *intrinsic* HBT parameters affecting Z'_{12}. In order to choose an initial value for L_{bx} and L_{ex}, the arbitrary assumption was made that $\mathrm{Im}[Z_{11}] \approx \omega(L_{bx}+L_{ex})$ and $\mathrm{Im}[Z_{12}] \approx \omega L_{ex}$, from which the two inductors were found as $L_{ex}=5$ pH and $L_{bx}=68.9$ pH. Similar to the discussion above regarding C_{p1}, C_{p2}, etc., these inductors can be distributed. For example, these inductors include the effect of the inductors of the *analytic* HBT-model, namely, L_b, L_{bp}, and L_{e1}. The initial values for L_{bx}, L_{bp}, and L_{b1} were, therefore, defined according to $L_{bx}+L_{bp}+L_{b1}=68.9$ pH. Similarly, the initial values for L_{ex} and L_{e1} were defined from $L_{e1}+L_{ex}=5$ pH. Finally, it must be noted that a zero value for L_{cx} was employed as the initial value since the imaginary parts of Z_{22} and Z_{21} did not exhibit a linear frequency dependence due to the strong effects of the collector–base capacitance on these parameters.

Other HBT-model parameters that need to be initialized are R_{b1}, R_{bp1}, R_c, and R_{e1}. Suitable initial values for these elements were obtained from the dc data and were discussed earlier. Other parameters like the phase delay τ_d, the pole of α', and f_a are chosen based on physical considerations derived from the device structure and material properties. Assuming an electron mobility in the base ($W_B = 700$ Å, $N_a = 5\times10^{19}$ cm^{-3}) of $\mu_n = 1000$ cm^2/V·s gives a diffusivity of $D_n = 0.0026$ m^2/s which results in a base transit time $\tau_B = W_B^2/2D_n = 0.95$ ps. Therefore, $f_a \equiv \frac{1}{2\pi\tau_B}$ was initialized with a value of 168 GHz. For the phase delay τ_d, a saturation velocity in the collector $v_s = 10^7$ cm/s was assumed. Given the collector thickness of $W_C = 0.7$ μm, τ_d was calculated for a completely depleted collector region by $\tau_d = 0.5W_C/v_s$, which resulted in a value of $\tau_d = 3.5$ ps. Both time constants were very close to the final values obtained for τ_d and τ_B under forward bias device operation as will be shown in the following sections.

V. HBT RF Parameter Extraction

The extraction procedure of HBT small-signal model parameters developed here combines both empirical optimization and analytical HBT-impedance-modeling procedures.

An overview of the proposed algorithm is shown in Fig. 6. For a given set of initial device parameters, the procedure is carried out in a self-consistent manner and at various phases. Initially, the parasitic impedances Z_{bx}, Z_{ex}, and Z_{cx} are calculated and subtracted from the measured Z-parameters, to obtain the Z'-shell parameters. The latter are then transformed to the corresponding Y'-shell parameters. Subsequently, the parasitic capacitances Y_{p1}, Y_{p2}, and Y_{px} are subtracted from the Y'-shell parameters. This results in the evaluation of the Y-parameters of the analytic HBT shell.

Once the network parameters of the *analytic* HBT shell have been obtained, the analytical expressions derived in [9] are employed in order to evaluate the impedance blocks of the HBT model. These are Z_{b1}, Z_{be}, Z_e, Z_{bc}, Z_c, and α', and are related to the H-parameters of the *analytic* HBT model by

$$Z_{b1} = \frac{H_{11}H_{22}-H_{12}H_{21}-H_{12}}{H_{22}} \tag{19}$$

$$Z_{\mathrm{bc}}+Z_c = \frac{1+H_{21}}{H_{22}} \tag{20}$$

$$Z_{\mathrm{be}}+Z_e = \frac{H_{12}}{H_{22}} \tag{21}$$

$$\alpha' Z_{\mathrm{bc}} = \frac{H_{21}+H_{12}}{H_{22}}. \tag{22}$$

According to the method in [9], all HBT parameters are determined by utilizing the frequency response of the above impedance blocks. In the case where the device parasitics are known, the latter approach can be applied directly, in order to evaluate the HBT elements. If, however, such parasitics are either not known or are not included in the model, direct application of the method in [9] may result in impedance blocks whose frequency dependence does not correspond to physically significant circuits. Such an example is the case of Z_c impedances corresponding to negative R_c values. The main idea of this paper is to evaluate these parasitics in order to obtain impedance blocks that correspond to realistic circuit blocks. Such evaluation has been implemented in a self-consistent manner: First, the impedance blocks of the *analytic* HBT obtained from (19) to (22) are fitted to practical circuits. For example, $Z_{\mathrm{be}}+Z_e$ is fitted to a circuit consisting of a series combination of impedances $R_{e1}+j\omega L_{e1}$ and $R_{\mathrm{be}}//(C_{\mathrm{BE}}+C_{\mathrm{JE}})$. The representation of all impedance blocks in terms of circuit elements can be seen in Fig. 3(a) and 3(b). If the fit of impedance blocks to physical circuitry is not satisfactory, the external parasitics are modified and the impedance blocks are re-evaluated. The procedure is iterated until convergence is achieved.

The evaluation of both the *analytic* HBT elements and the external parasitics in the present procedure is achieved, mainly through optimization. It differs, however, from a completely empirical optimization procedure. Use of analytic expressions to calculate the four HBT-model impedance blocks implies that the model parameters of the *analytic* HBT shell are sorted and optimized in independent groups (except parameters related to the $\alpha' Z_{\mathrm{bc}}$ and $Z_{\mathrm{bc}}+Z_c$ blocks). Each group employs a simple optimization goal that relates a limited set of parameters to the frequency response of an analytically calculated impedance block. Such a goal can be defined, for example, to match the frequency response of the modeled with the analytically calculated impedance block (i.e., *impedance block conditioned optimization*). The modeled impedance blocks can be easily identified from Fig. 3(a). The *measured* impedance blocks are obtained from the deembeded H-parameters of the *analytic* HBT model using (19)–(22). Thus, each time an element is modified by the gradient optimizer, only one (two) impedance block(s) is (are) changed leading to modification of only one (two) goal(s). In a completely empirical optimization, changing one element would cause modification of all four goals (usually involving the modeled and measured S-parameters). This implies a distinct advantage of the new method over the completely empirical procedure, namely, using the present scheme the user is able to identify and

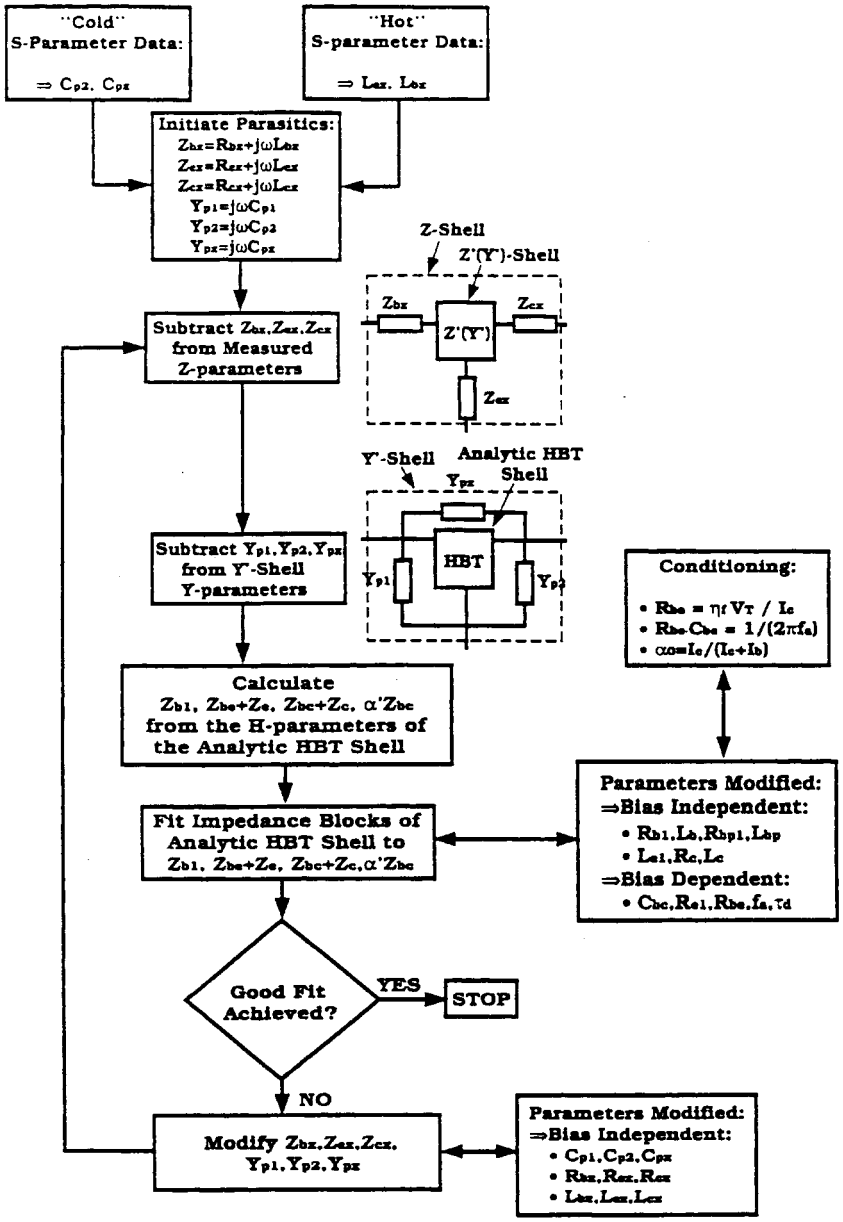

Fig. 6. Procedure flowchart for the evaluation of HBT small-signal equivalent circuit parameters.

even manually modify the elements of the HBT model which cause a misfit between the measured and modeled HBT characteristics.

The above conceptual difference between this paper's method and a completely empirical optimization does not necessarily imply better performance of the former method since problems related to the existence of multiple sets of parameters leading to best fits still can exist. However, the user has better control over the fitting variables in the former case, which implies a more systematic and reliable HBT parameter evaluation.

In order to enhance the physical interpretation of the obtained results, the above-established approach was extended and the information presented here is based on the use of the following procedures:

- simultaneous use of multibias S-parameter data files in the optimization cycle;
- conditioning of some elements according to dc and RF HBT operation.

The above constraints imply the separation of the unknown parameters into bias-dependent and bias-independent parameters. The bias-dependent parameters are shown in Fig. 6 and are α_0, $C_{\rm BE}+C_{\rm JE}$, $C_{\rm bc}$, R_{e1}, $R_{\rm be}$, f_a, and τ_d. The relations used to condition $R_{\rm be}$ and f_a were

$$R_{\rm be}=\frac{\eta_f V_T}{I_C} \tag{23}$$

$$C_{\rm BE}+C_{\rm JE}=\frac{1}{2\pi f_a R_{\rm be}} \tag{24}$$

and

$$\alpha_0=\frac{I_C}{I_C+I_B}. \tag{25}$$

It must be noted here that both $R_{\rm be}$ and α_0 are affected by thermal effects. However, while α_0 is directly obtained from

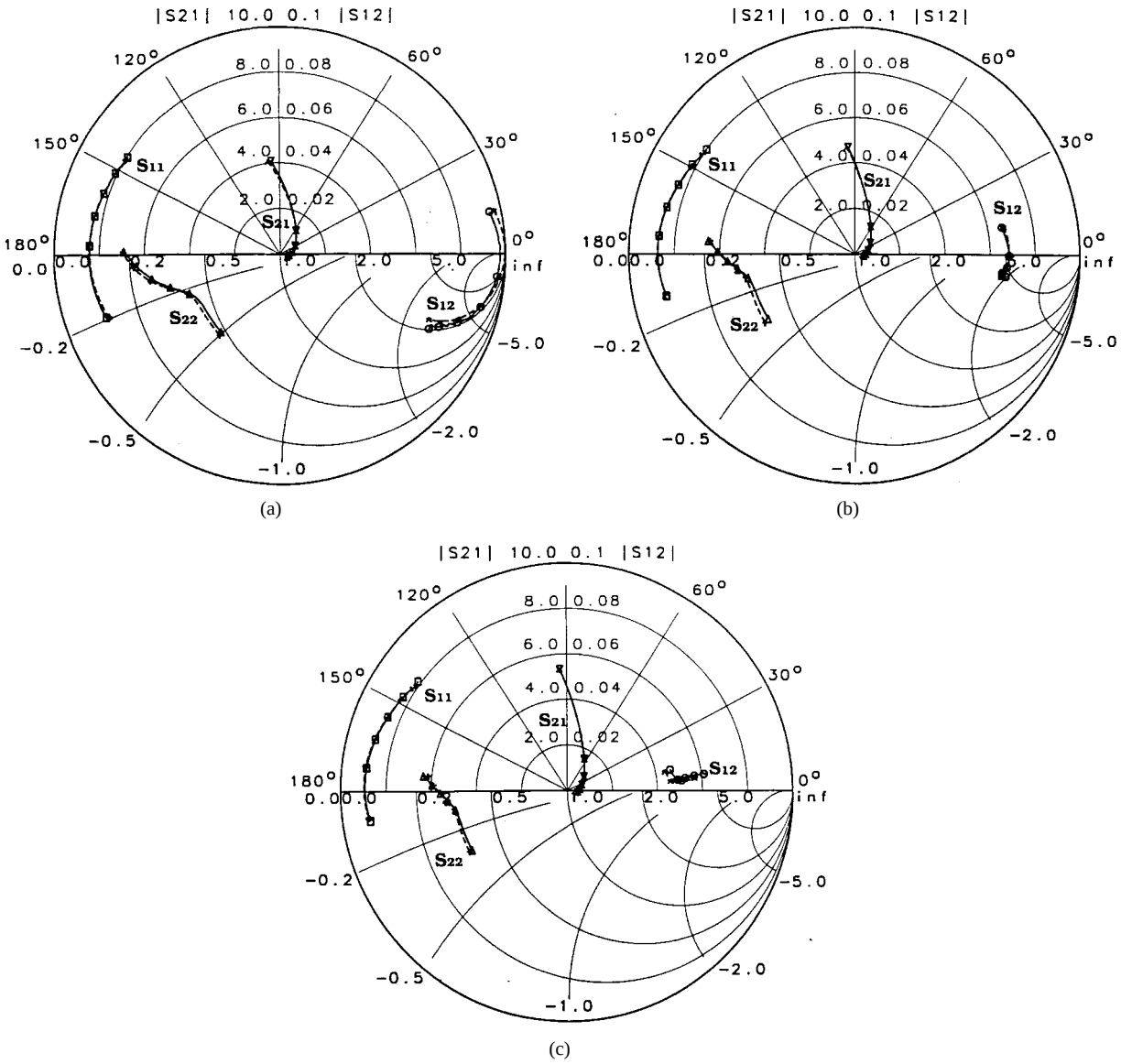

Fig. 7. (a) Measured (solid lines) and modeled (dashed lines) S-parameters for bias operating condition $I_C = 11$ mA and $V_{\rm CE} = 2.2$ V. (b) Measured (solid lines) and modeled (dashed lines) S-parameters for bias operating condition $I_C = 23.8$ mA and $V_{\rm CE} = 2.2$ V. (c) Measured (solid lines) and modeled (dashed lines) S-parameters for bias operating condition $I_C = 60.3$ mA and $V_{\rm CE} = 2.2$ V.

TABLE II
SETS OF BIAS OPERATING CONDITIONS USED IN OPTIMIZATION

	Bias Set A	Bias Set B
I_C^1 (mA)	11	21.4
V_{CE}^1 (V)	2.2	5.2
I_C^2 (mA)	23.8	47.8
V_{CE}^2 (V)	2.2	5.2
I_C^3 (mA)	60.3	60.3
V_{CE}^3 (V)	2.2	2.2

the measured dc I_C–$V_{\rm CE}$ characteristics, calculation of $R_{\rm be}$ requires the knowledge of device temperature T. Although this paper assumes isothermal device characteristics ($T = 300$ K), an HBT large-signal model incorporating self-heating effects could provide more accurate conditioning relations, especially at bias conditions exhibiting significant self-bias effects and for larger size power devices. This could lead to smaller ambiguities of extracted parameters such as R_E. Finally, it must also be recalled that initialization of some of the parameters, as described in the previous section, further enhances the physical validity of the obtained results. Thus, the solutions obtained by the procedures described in this paper are very likely to lead to unique solutions for representing the HBT model.

VI. RESULTS AND DISCUSSION

The new approach was implemented in the commercial microwave simulator LIBRA and implements a simultaneous optimization of S-parameter data measured at three different bias points. Altogether, two optimizations (A and B) were carried out in the frequency range of 3–40 GHz, each involving a set of three bias points. Table II shows the dc-bias operating conditions for which the device S-parameter data were measured and HBT parameters were evaluated.

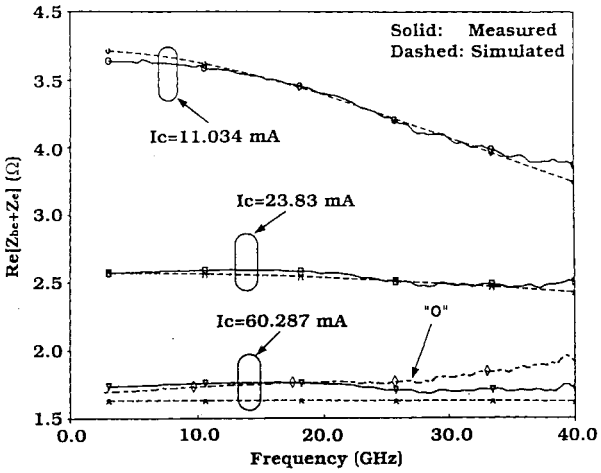

(a)

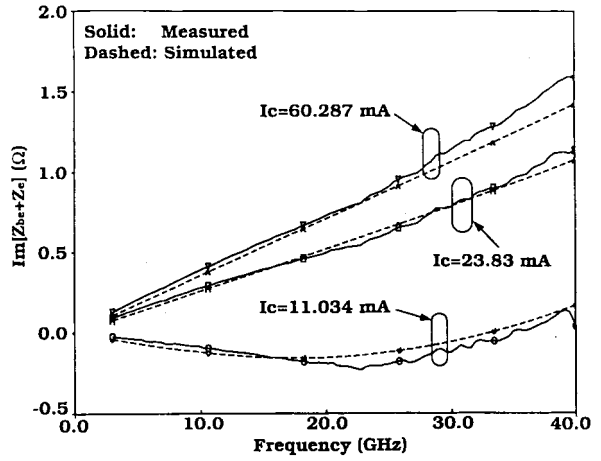

(b)

Fig. 8. (a) Frequency dependence of $\mathrm{Re}[Z_{\mathrm{be}}+Z_e]$ at different bias operating points (Bias Set A) The curve marked 0 corresponds to a solution obtained from the original approach proposed by the authors [9], [10]. (b) Frequency dependence of $\mathrm{Im}[Z_{\mathrm{be}}+Z_e]$ at different bias operating points (Bias Set A).

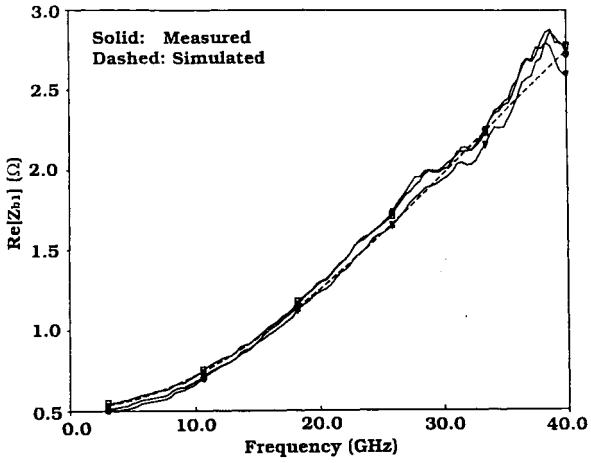

Fig. 9. Frequency dependence of $\mathrm{Re}[Z_{b1}]$ at different bias operating points (Bias Set A). The measured quantities (solid lines) are bias independent.

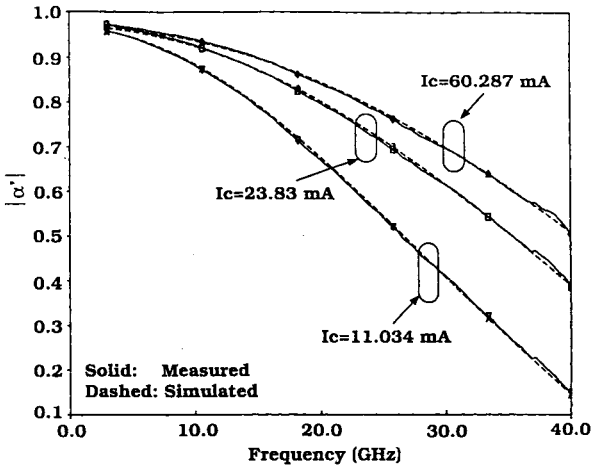

Fig. 10. Frequency dependence of $|\alpha'|$ at different bias operating points (Bias Set A).

The measured and modeled S-parameters for the bias conditions of Bias Set A of Table II are shown in Fig. 7(a)–(c). As one observes, the fit between the measured and modeled data is excellent. The various impedance blocks used to establish the optimization goals of the present method can also be calculated. Fig. 8(a) and (b) show the real and imaginary parts of $Z_{\mathrm{be}}+Z_e$ as a function of frequency for the three bias conditions considered in the optimization. Very good fit is again observed between the measured (i.e., the analytically deembeded quantities) and the modeled results. One notices also that $\mathrm{Re}[Z_{\mathrm{be}}+Z_e]$ decreases with increasing frequency. This trend results from the physical interpretation of the emitter–base junction as a series connection of $R_{e1}+j\omega L_{e1}$ with $R_{\mathrm{be}}//(C_{\mathrm{BE}}+C_{\mathrm{JE}})$. Failure to incorporate device parasitics into the model could lead this component into an increasing behavior with respect to frequency which is not physical and does not correspond to the assumed representation of the junction. This is a result of the principles of the present method, namely, the physical interpretation of the impedance blocks is enforced during optimization. To demonstrate the superiority of the approach described in this paper, the authors included in Fig. 8(a) the results obtained using their originally proposed techniques [9], [10], as applied to the same HBT. $\mathrm{Re}[Z_{\mathrm{be}}+Z_e]$ is shown here to follow a nonphysical behavior as obtained with the old technique since it is found to increase with frequency.

Fig. 9 shows the real part of Z_{b1}. Z_{b1} is a bias-independent quantity. As one observes, the measured $\mathrm{Re}[Z_{b1}]$ quantities are in excellent agreement with the modeled one. Similar agreement was found for the imaginary part of Z_{b1}.

The frequency dependence of the transport factor $|\alpha'|$ is shown in Fig. 10 for different bias operating points. Excellent fit is observed between measured and modeled results. A comparison of those results with data obtained for $|\alpha'|$ as evaluated using the authors' original approach again confirms the superiority of the new technique since the old approach results in values of $|\alpha'|$ greater than 1, which increase with frequency. Finally, the measured and modeled $|h_{21}|$ and maximum available gain $G_{\max}$ are shown in Fig. 11(a) and (b), respectively, for the three different bias conditions. Their excellent fit further verifies the validity of the developed method.

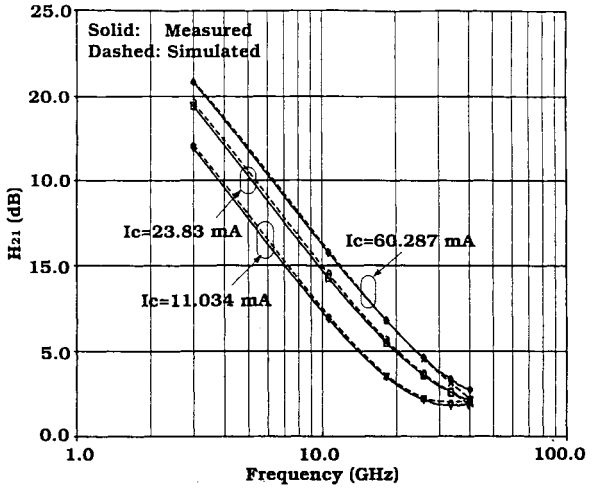

(a)

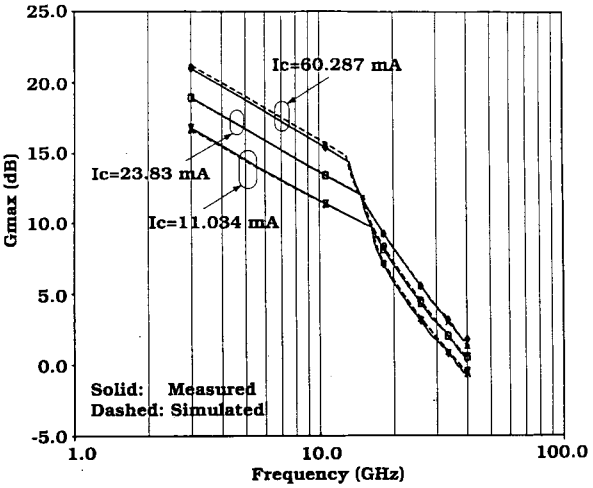

(b)

Fig. 11. (a) Frequency dependence of $|h_{21}|^2$ at different bias operating points (Bias Set A). (b) Frequency dependence of $G_{\max}$ at different bias operating points (Bias Set A).

To further evaluate the validity and suitability of the present approach, the same procedure was applied for a different set of bias operating conditions, defined in Table II as Bias Set B, involving not only data at different currents but also at different $V_{\rm CE}$ operating conditions. An accuracy of four decimal points was maintained in all data, discussed below, to comply with the even higher resolution employed in the measured dc and HF data. As for the case of Bias Set A, the fit between measured and simulated S-parameters and impedance blocks was excellent for each set of bias points. Ideally, since the parasitics should maintain a physically meaningful character, these bias-independent elements should be identical for all three sets. Table III shows all these elements for each set of bias points. As one observes, the variation of these parameters is indeed small for the two different bias sets suggesting the validity of the proposed approach. Moreover, some of the elements have almost negligibly small values and were, therefore, set to zero. The small variation observed in these data appears to result from statistical errors inherent in the employed optimization procedures, as well as the omission of self-heating effects from the modeling approach.

TABLE III
DEPENDENCE OF BIAS-INDEPENDENT HBT PARAMETERS ON BIAS SET

Parameter	Bias Set A	Bias Set B
C_{p1} (fF)	0.0	0.0
C_{p2} (fF)	113.9	109.7
C_{px} (fF)	0.0	0.0
R_{bx} (Ω)	0.0	0.0
R_{ex} (Ω)	0.0	0.0
R_{cx} (Ω)	0.21	0.32
L_{bx} (pH)	0.4	0.0
L_{ex} (pH)	1.1	0.0
L_{cx} (pH)	36.0	39.8
R_{b1} (Ω)	0.51	0.5
L_b (pH)	48.7	49.4
R_{bp1} (Ω)	6.94	6.6
L_{bp} (pH)	18.9	18.3
L_{e1} (pH)	5.8	8.6
R_c (Ω)	0.013	0.0
L_c (pH)	22.6	18.6

It must be noted here that the final estimates for $L_{bx}+L_{bp}+L_{b1}$ and $L_{ex}+L_{e1}$ are close to the initial estimates determined in the previous section. However, $R_{bx}+R_{b1}$ and $R_{cx}+R_c$ differ from the values determined from the dc measurements (R_B and R_C, respectively) shown in Table I. One reason for this discrepancy may be attributed to the distributed nature of the base and collector contacts causing a frequency dispersion of the real part of the base and collector impedances. Another reason may be due to the fact that the dc measurements were carried out using a different experimental setup than the HF measurements; thus introducing different access resistances between the instrument and the device which are not calibrated out to the same degree. Finally, it was observed that the optimization of the HBT equivalent circuit was less sensitive on R_C or R_B compared to R_{e1}, which may also imply some uncertainty in the values obtained from the present procedure.

The bias dependence of the time constants τ_d and $\tau_a \equiv \frac{1}{2\pi f_a}$ is shown in Fig. 12 for the case of Bias Set A. As one observes, τ_a can be directly fitted to an expression $\tau_a = a/I_C$, where $a = 33$ ps·mA. τ_d shows a weaker bias dependence and can be fitted to $\tau_d = d_1 \cdot I_C + d_2$ where $d_1 = 0.011$ ps/mA and $d_2 = 2.84$ ps.

All bias dependent parameters are shown in Table IV. One sees from this table that $C_{\rm bc}$ shows a decrease with increasing current (Bias Set 1). This variation of $C_{\rm bc}$ with current was allowed in this paper's procedure to account for the possible modification of the collector–base space–charge layer by the injected carriers. For an n-type doped collector, the peak electric field in the collector is located on the base side of the collector. As current injection increases, the peak electric field is lowered and the electric field on the sub-collector side increases. The latter change causes electrons in the collector–sub-collector interface to move farther toward the sub-collector region. That, in turn, translates to a widening of the collector space–charge region and, consequently, a lowering of the collector–base capacitance as the current injection increases. At high currents, however, the opposite

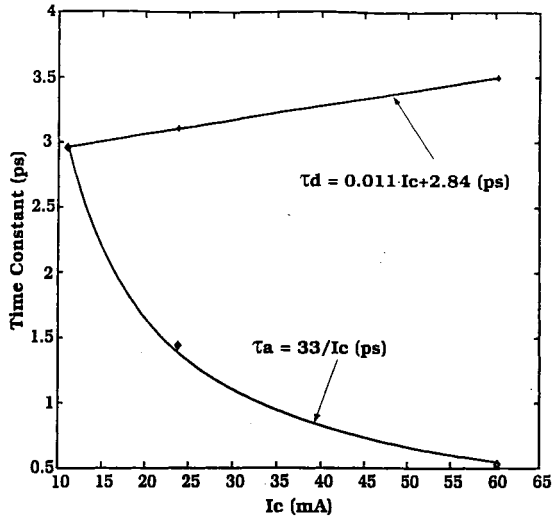

Fig. 12. Bias dependence of time constants $\tau_a = 1/2\pi f_a$ and τ_d for operating conditions in Bias Set A. Both constants can be fit to closed-form expressions.

TABLE IV
BIAS DEPENDENCE OF HBT MODEL PARAMETERS

	Bias Set A			Bias Set B		
I_C (mA), V_{CE} (V)	11,2.2	23.8,2.2	60.3,2.2	21.4,5.2	47.8,5.2	60.3,2.2
α_0	0.965	0.9675	0.9679	0.9639	0.9598	0.9679
R_{be} (Ω)	2.7514	1.274	0.5036	1.4193	0.635	0.5036
R_{e1} (Ω)	1.4681	1.3	1.1273	1.5154	1.292	1.4314
C_{bc} (fF)	261.5	257.7	236.5	220.4	211.9	234.6
f_a (GHz)	53.99	110.5468	299.179	72.387	100.43	244.0
τ_d (ps)	2.9628	3.1067	3.4985	4.4216	4.5717	3.4381

effect will take place. As the current increases, the electric field in the collector is inverted, i.e., its peak is shifted toward the sub-collector. This gives rise to base pushout effects, which effectively shrinks the width of the collector space–charge region and consequently causes a rise of $C_{\rm bc}$ with the increasing current. Such modifications of $C_{\rm bc}$ by current injection is stronger for low-doped collector regions such as, for example, the transistors of this work, which were n-type doped at $3{\cdot}10^{16}$ cm^{-3}. Self-heating effects may also play a role in the bias dependence of $C_{\rm bc}$. Such effects were significant for the device under investigation but were not considered here. The variation of $C_{\rm bc}$ with V_{CE} can also be seen from Table IV. As expected, $C_{\rm bc}$ decreases as $V_{\rm CE}$ increases, due to the collector space–charge region widening by increased reverse voltage.

Finally, comparing columns four and seven of Table IV, one identifies some uncertainty of the values of f_a, which is of the order of 55 GHz. Such uncertainty is, however, smaller for the emitter resistance R_{e1} and is of the order of 0.3 Ω. Moreover, one observes in Table IV that R_{e1} decreases with I_C. Such a trend could be the result of thermal effects. As was discussed in previous sections, in the presence of self-heating effects, the voltage drop across the intrinsic base–emitter junction given in (1) can be written as

$$V_{\rm BE,int} = V_{\rm BE} - I_C(R_E - \delta R_{\rm th} V_{\rm CE}) - I_B(R_E + R_B - \delta R_{\rm th} V_{\rm BE}). \quad (26)$$

Increasing I_C causes the dc dissipated power to increase. The thermal resistance usually is a nonlinear function of the dissipated power and increases as this power increases. Therefore, the effective emitter series resistance, given by $R_{E,\rm eff} \equiv R_E - \delta R_{\rm th} V_{\rm CE}$ will decrease as I_C increases. Subsequently, such a trend will be reflected on the estimated parameter R_{e1} (and possibly R_{ex}) determined for the HBT small-signal model [see Fig. 3(a)]. Using values of $\delta = 1.37$ mV/K, $V_{\rm CE} = 2.2$ V, and the decrease of $R_{E,\rm eff}$ given for a change of I_C from 10 to 60 mA in Bias Set A (i.e., $\Delta R_{E,\rm eff} = 0.34\ \Omega$), one can calculate the variation of $R_{\rm th}$ from $\Delta R_{E,\rm eff} = \delta V_{\rm CE} \Delta R_{\rm th}$ resulting in $\Delta R_{\rm th} = 112$ K/W. Uncertainties in the model parameters can possibly be alleviated by introducing additional constraints for these parameters based on physics-based numerical device simulation rather than the closed-form physical expressions such as the one used earlier for the initial estimation of f_a.

VII. CONCLUSION

A new technique for the prediction of dc and RF HBT-model parameters was developed. Dc parameters such as α_0 are $R_{\rm be}$ used as constraints in RF simulations while others (R_B, R_E, and R_C) are used as initial values. All HF parameters are evaluated by employing, in part, empirical optimization and analytical evaluations. The optimization goals are defined with respect to device impedance blocks calculated from an analytical model. Simulations were simultaneously carried out for multibias S-parameter data. Excellent fit was observed between experimental and modeled S-parameter over a wide range of bias operating conditions.

REFERENCES

[1] B. Bayraktaroglu, "GaAs HBT's for microwave integrated circuits," *Proc. IEEE*, vol. 81, pp. 1762–1785, Dec. 1993.
[2] P. M. Asbeck, F. M. C. Chang, K. C. Wang, G. J. Sullivan, and D. T. Cheung, "GaAs-based heterojunction bipolar transistors for very high performance electronic circuits," *Proc. IEEE*, vol. 81, pp. 1709–1726, Dec. 1993.
[3] D. Costa, W. U. Liu, and J. S. Harris, "Direct extraction of the AlGaAs/GaAs heterojunction bipolar transistor small-signal equivalent circuit," *IEEE Trans. Electron Devices*, vol. 38, pp. 2018–2024, Sept. 1991.
[4] D. W. Wu and D. L. Miller, "Unique determination of AlGaAs/GaAs HBT's small-signal equivalent circuit parameters," in *15th IEEE GaAs IC Symp. Dig.*, San Jose, CA, Oct. 10–13, 1993, pp. 259–262
[5] R. J. Trew, U. K. Mishra, W. L Pribble, and J. F. Jensen, "A parameter extraction technique for heterojunction bipolar transistors," in *IEEE MTT-S Symp. Dig.*, Long Beach, CA, June 13–15, 1989, pp. 897–900.
[6] S. Lee and A. Gopinath, "New circuit model for RF probe pads and interconnections for the extraction of HBT equivalent circuits," *IEEE Electron Device Lett.*, vol. 12, pp. 521–523, Oct. 1991.
[7] ——, "Parameter extraction technique for HBT equivalent circuit using cutoff mode measurement," *IEEE Trans. Microwave Theory Tech.*, vol. 40, pp. 574–577, Mar. 1992.
[8] S. Lee and S. W. Kang, "A parameter extraction method using cutoff measurement for a large-scale HSPICE model of HBT's," *IEEE Trans. Electron Devices*, vol. 41, pp. 112–114, Jan. 1994.
[9] D. R. Pehlke and D. Pavlidis, "Evaluation of the factors determining HBT high-frequency performance by direct analysis of S-parameter data," *IEEE Trans. Microwave Theory Tech.*, vol. 40, pp. 2367–2373, Dec. 1992.
[10] A. Samelis, D. R. Pehlke, and D. Pavlidis, "Volterra series based nonlinear simulation of HBT's using analytically extracted models," *Electron. Lett.*, vol. 30, no. 13, pp. 1098–1100, June 1994.
[11] U. Schaper and B. Holzapfl, "Analytical parameter extraction of the HBT equivalent circuit with T-like topology from measured S-parameter

data," *IEEE Trans. Microwave Theory Tech.*, vol. 43, pp. 493–498, Mar. 1995.
[12] S. J. Spiegel, D. Ritter, R. A. Hamm, A. Feygenson, and P. R. Smith, "Extraction of the InP/GaInAs heterojunction bipolar transistor small-signal equivalent circuit," *IEEE Trans. Electron Device Lett.*, vol. 42, pp. 1059–1064, June 1995.
[13] C. J. Wei and J. C. M. Hwang, "Direct extraction of equivalent circuit parameters for heterojunction bipolar transistors," *IEEE Trans. Microwave Theory Tech.*, vol. 43, pp. 2035–2040, Sept. 1995.
[14] M. E. Hafizi, C. R. Crowell, and M. E. Grupen, "The dc characteristics of GaAs/AlGaAs heterojunction bipolar transistors with application to device modeling," *IEEE Trans. Electron Device Lett.*, vol. 37, pp. 2121–2129, Oct. 1990.
[15] S. Tiwari, *Compound Semiconductor Device Physics*. New York: Academic Press, 1992, ch. 7, pp. 550–703.
[16] P. C. Grossman and J. C. Choma Jr., "Large signal modeling of HBT's including self-heating and transit time effects," *IEEE Trans. Microwave Theory Tech.*, vol. 40, pp. 449–464, Mar. 1992.

Apostolos Samelis was born in Kalamata, Greece, on November 8, 1967. He received the Diploma in electrical engineering (with distinction) in 1990 from the University of Patras, Greece, and the M.S. and Ph.D. degrees in electrical engineering from the University of Michigan, Ann Arbor, in 1991 and 1996, respectively. His Ph.D. work dealt with the development of bias-dependent HBT small-signal equivalent circuit parameter extraction techniques, device design-based analysis, and optimization of intermodulation distortion in HBT's, the analysis of thermal effects and breakdown in HBT's using physics-based and circuit-oriented large-signal models, and the investigation of the power, intermodulation, and efficiency trade-offs of power HBT's.

In April 1996, he joined Rockwell Semiconductor Systems, Newbury Park, CA, where he is currently working on HBT large-signal modeling and characterization.

Dimitris Pavlidis (S'73–M'76–SM'83–F'93) received the B.Sc. degree in physics from the University of Patras, Patras, Greece, in 1972, and the Ph.D. degree from the University of Newcastle, Newcastle-upon-Tyne, U.K., in 1976. He continued as a Post-Doctoral Fellow at Newcastle until 1978, engaged in work on microwave semiconductor devices and circuits.

Since 1986, he has been Professor of electrical engineering and computer science at the University of Michigan, Ann Arbor. In 1978, he joined the High Frequency Institute of the Technical University of Darmstadt, Germany, working on III-V devices and establishing a new semiconductor technology facility. In 1980, he worked at the Central Electronic Engineering Research Institute, Pilani, India, as a UNESCO consultant. From 1980 to 1985, he was Engineer and Manager of the GaAs Monolithic Microwave Integrated Circuits (MMIC's) Department of Thomson-CSF, Corbeville, France. Since 1986, he has been involved in research on heterostructure devices and materials at the University of Michigan. His materials research covers InP and Nitride-based materials using Metalorganic Chemical Vapor Deposition (MOCVD). His work in the above areas has been reported in numerous papers and reports, and he holds six patents.

Prof. Pavlidis was awarded the European Microwave prize for his work in InP-based monolithic integrated HEMT amplifiers in 1990. In 1991, he received the decoration of "Palmes Académiques" in the order of Chevalier by the French Ministry of Education for his work in education. In 1992, he received the Japan Society of Promotion of Science Fellowship for Senior Scientists/Professors from the Japanese government and the Humbolt Research Award for Distinguished Senior U.S. Scientists.